Nucleation and growth kinetics of CaCO3 crystals in the presence of foreign monovalent ions

Journal of Crystal Growth 578 (2022) 126406

Contents lists available at ScienceDirect

Journal of Crystal Growth

journal homepage: www.elsevier.com/locate/jcrysgro

Nucleation and growth kinetics of $CaCO_3$ crystals in the presence of foreign monovalent ions

Freddy Liendo, Mara Arduino, Fabio A. Deorsola, Samir Bensaid *

Department of Applied Science and Technology, Politecnico di Torino, Corso Duca degli Abruzzi, 24, 10129 Torino, Italy

ARTICLE INFO

Communicated by Alexander van Driessche

Keywords:
A1. Crystal morphology
A1. Crystal structure
A1. Growth models
A1. Nucleation
B1. Calcium compounds
B1. Salts

ABSTRACT

The aim of this work is to study the effect of the presence of different monovalent ions (Na^+, NH_4^+ and K^+) on the nucleation and growth rates of $CaCO_3$ precipitation. There is currently great interest in the precipitation of $CaCO_3$ particles reusing CO_2 rich flue gases and calcium-rich wastes, which implies the presence of foreign ions that can affect the crystallization process. Unseeded and seeded tests were carried out in a batch system to estimate the nucleation and growth kinetics, respectively. Tests with Na_2CO_3 and $CaCl_2$ as precursors led to the classical calcite crystallization mechanism via vaterite formation at high supersaturations. On the other hand, the use of $(NH_4)_2CO_3$ entailed lower pH and the presence of NH_4^+, which stabilized the vaterite and avoided its transformation into stable calcite crystals. Thus, faster nucleation kinetics by using Na_2CO_3 were obtained. To estimate the growth rate, tests with two initial seed loadings and types (micro and nano seed) were performed. The growth rate increased with the crystal size and decreased with the magma density. The results indicate that the ion effect on the growth rate seems to be related to the ionic radius of the foreign ion.

1. Introduction

The precipitation of $CaCO_3$ crystals is of considerable interest to researchers nowadays. The size and morphology of these crystals are easily tuneable through the synthesis method [1–3]. Thus, because of their non-toxicity and biocompatibility, according to their morphological characteristics they are widely employed in different fields [1,4,5]. $CaCO_3$ synthesis can be controlled in order to tailor these morphological characteristics for the final purpose of the crystals. Hence, the study of the precipitation mechanism and kinetic of $CaCO_3$ is important. The precipitation process takes place due to the reaction between calcium and carbonate ions. Moreover, other ionic interactions are involved in this process and could seriously affect the precipitation pathway.

Equations (1)–(14) highlight all these ionic interactions. From the carbonic species and water equilibria to the ion-pair and solid-liquid phase equilibria. The reactions involving the formation of $CaOH^+$ and $CaHCO_3^-$ ions could be neglected since the equilibrium constants do not favor their formation and their concentration are negligible for the ionic balance[6–8]. Thus, several factors can affect the precipitation process and the predominant one is the supersaturation ratio (S) of $CaCO_3$, which is the driving force of nucleation and growth phenomena and is defined by eq. (15).

(a) Carbonic species and water equilibria

$$CO_{2_{(g)}} \rightleftarrows CO_{2_{(aq)}} \qquad K_L a \qquad (1)$$

$$CO_{2_{(aq)}} + H_2O \rightleftarrows H_2CO_3 \qquad K_h \qquad (2)$$

$$H_2CO_3 \rightleftarrows HCO_3^- + H^+ \qquad K_{a1} \qquad (3)$$

$$HCO_3^- \rightleftarrows CO_3^{2-} + H^+ \qquad K_{a2} \qquad (4)$$

$$H_2O \rightleftarrows H^+ + OH^- \qquad K_w \qquad (5)$$

(b) Ion-pair equilibria

$$H^+ + X^- \rightleftarrows HX \qquad K_a \qquad (6)$$

$$B^+ + OH^- \rightleftarrows BOH \qquad K_b \qquad (7)$$

$$Ca^{2+} + HCO_3^- \rightleftarrows CaHCO_3^+ \qquad K_{CaHCO_3^+} \qquad (8)$$

$$Ca^{2+} + OH^- \rightleftarrows CaOH^+ \qquad K_{CaOH^-} \qquad (9)$$

* Corresponding author.
E-mail address: samir.bensaid@polito.it (S. Bensaid).

https://doi.org/10.1016/j.jcrysgro.2021.126406
Received 5 February 2021; Received in revised form 21 October 2021; Accepted 24 October 2021
Available online 29 October 2021

$$Ca^{2+} + CO_3^{2-} \rightleftarrows CaCO_3^0 \qquad K_{CaCO_3^0} \qquad (10)$$

(c) Solid-Liquid phase equilibria

$$CaX_{2(s)} \rightleftarrows Ca^{2+} + 2X^- \qquad K_L a \qquad (11)$$

$$B_2CO_{3(s)} \rightleftarrows 2B^+ + CO_3^{2-} \qquad K_{sp1} \qquad (12)$$

$$Ca^{2+} + OH^- \rightleftarrows Ca(OH)_{2(s)} \qquad K_{sp2} \qquad (13)$$

$$Ca^{2+} + CO_3^{2-} \rightleftarrows CaCO_{3(s)} \qquad K_{sp-CC} \qquad (14)$$

$$S = \sqrt{\frac{aCa^{2+}aCO_3^{2-}}{k_{sp}}} \qquad (15)$$

Where k_{sp} is the solubility product of the considered $CaCO_3$ phase, while aCa^{2+} and aCO_3^{2-} are the activity of the calcium and carbonate ions, respectively. The solubility product varies according to the $CaCO_3$ phase and is temperature-dependent. The activity of the ions is affected by the operating conditions, such as temperature, pH, and ionic strength, according to the Debye-Huckel law. Hence, the supersaturation ratio is similarly affected. It follows that the factors mentioned above must considerably influence the precipitation kinetic. Thus, different crystalline phases of $CaCO_3$, such as calcite, vaterite and aragonite, can be obtained. Calcite is the most stable phase of the $CaCO_3$ at any temperature, while vaterite and aragonite are metastable phases. The mechanism of the $CaCO_3$ crystallization has been previously studied by Rodriguez-Blanco et al.[9]. They studied the $CaCO_3$ precipitation starting from a $Na_2CO_3/CaCl_2$ mixture and concluded that the process could be divided into two main stages. The first stage is characterized by the transformation of the initially produced unstable Amorphous Calcium Carbonate (ACC) in a metastable phase like vaterite, which subsequently turns into stable calcite in the second stage. This research is in good agreement with other works: for instance, Bots et al. studied the mechanistic insights of the crystallization of ACC to vaterite and divided the process into three stages: ACC formation and vaterite spherulitic growth is the first stage, while the second and third stage concern the vaterite growth and ripening. They also studied the effect of the presence of SO_4^{2-} on the growth of these crystals, which reduces the rate of ripening and produces smaller crystals[10]. Bots et al. combined their results with those obtained by Rodriguez-Blanco et al., allowing them to elucidate the full abiotic transformation mechanism from ACC to calcite via vaterite[10]. The transformation of vaterite to calcite has also been studied by Ogino et al., who determined that it proceeds through a dissolution of the vaterite followed by calcite growth, which is the rate-determining step[11].

Recently, there has been a growing interest in merging the need for CO_2 emissions mitigation with the production of high added-value compounds. Calcium carbonate production is proving to be a promising route in carbon capture and utilization technologies. Different strategies have been studied to fulfil this scope, but many of them involve the use of chemicals for the CO_2 absorption from the flue gases [12] or the extraction of calcium sources from minerals or alkaline industrial wastes such as steel slags, fly ashes, waste cement, blast furnace slags and salty waters[13,14]. The use of chemicals or wastes implies the presence of foreign ions in solution such as Cl^-, SO_4^{2-}, Na^+, NH_4^+, K^+ and Mg^{2+}, which can affect the $CaCO_3$ nucleation and growth mechanism. Thus, controlling the crystal phase, morphology, and crystal size distribution is fundamental [15].

Mg^{2+} ions are highly present when calcium is extracted from steel slag [16] and minerals such as wollastonite and merwinite [16–18]. Several researchers have studied the Mg^{2+} ion effects on the precipitation of $CaCO_3$ [19–23]. These researchers agree that magnesium influences the precipitation process and promotes metastable aragonite over calcite and vaterite [23–26]. The effect is similar for different synthesis methods: the spontaneous precipitation reaction, slow carbonation and the carbonation process [22,26,27]. Potassium ions are known to control the crystal morphology. In their presence, rhombohedral calcite crystals are stabilized, while in the copresence of K^+ and Mg^{2+} ions, the formation of distinct aragonite needles and monohydrocalcite spherulites can be observed.[15]. Ammonium chloride has previously been used as solvent in calcium extraction from steelmaking slags [28,29]. Also, ammonia is widely employed to promote CO_2 absorption in carbonation processes [30]. Therefore, the effect of ammonium should also be studied. Some studies have been developed with this purpose, which reported that ammonia promotes metastable vaterite formation regardless of the synthesis method under certain conditions[30–34]. However, the study of the effect of ammonium ions on the precipitation kinetics could be deepened as well as the effect of sodium, potassium and chloride ions, since they are highly present in different types of wastes. Wastes such as oil shale ash collected from pulverized firings and fluidized bed combustion boilers [35], brines originated from underground saline aquifers and brought to the surface via oil and gas reservoirs[14], and brines discharged from seawater desalination plants [36,37] have all been employed as calcium sources and provide high Na^+, Cl^- and K^+ content.

This work aims to study the effects of the supersaturation ratio and the presence of different ions, especially the monovalent ions NH_4^+, Na^+ and K^+, on nucleation and growth kinetics. It further aims to study the effect of the morphology and size of the crystals on the growth kinetics through seeded experiments. This study could be highly useful for predicting the precipitation process based on the raw material employed. In such a way, the process could be controlled in order to obtain crystals with tuned characteristics.

1.1. Population balance equation

In a batch system, a general Population Balance Equation (PBE) can be expressed according to eq. (16).

$$\frac{\partial n}{\partial t} + \nabla \cdot \left(\vec{V} n\right) = \dot{B} - \dot{D} \qquad (16)$$

where n is the number density (#/m^3 of solution), $\dot{B}$ and $\dot{D}$ are the birth and death of crystals respectively due to aggregation and breakage phenomena. For the problem of a batch reactor (uniform and non-stationary) discussed by Core and Mulligan [38], the PBE becomes

$$\frac{\partial n}{\partial t} + \frac{\partial (Gn)}{\partial L} = \dot{B} - \dot{D} \qquad (17)$$

where G is the crystal growth rate. In this study, agglomeration and breakage phenomena can be neglected since the system is under continuous stirring, but not under high-stress conditions, which could generate crystals breaking, thus, $\dot{B}$ and $\dot{D}$ are not present in the PBE. In addition, size-independent growth and no crystal growth rate dispersion were assumed; therefore, the PBE is simplified as shown in eq. (18).

$$\frac{\partial n}{\partial t} + G\frac{\partial n}{\partial L} = 0 \qquad (18)$$

The size-independent growth assumption is widely employed to study the growth kinetics of crystals precipitation since the crystal growth is independent of crystal size per se[39]. Nonetheless, the crystal size has an apparent effect because larger crystals that have a higher settling velocity show a higher relative crystal-solution velocity. The relative crystal-solution velocity is the ratio between the crystal velocity and the bulk solution velocity. The crystal velocity depends on the crystal mass, and thus on its size. In fact, Mydlarz and Jones[40] concluded that the use of size-dependent growth models with two-three

parameters allowed them to improve the correlation to experimental data, particularly for large crystals ($d_p > 1000$ μm, i.e. much larger than our crystals in study). Despite these assumptions being valid under the test conditions, they will be verified and validated in this paper.

1.1.1. Nucleation

Nucleation consists of a first-order phase transition where a new phase is formed (solid), starting from an old one (liquid). The nucleation occurs by forming small metastable clusters inside the liquid phase, which grow until reaching a critical size and an energetic barrier is overcome, giving place to the formation of a stable nucleus.

According to the classical nucleation theory[41], Homogeneous nucleation takes place owing to elevated supersaturations. On the other hand, heterogeneous nucleation is induced by the presence of surfaces that act as "active sites", such as foreign crystals.

According to this theory, both the homogeneous and the heterogeneous nucleation rate can be expressed through the Arrhenius law, respectively through the eq. (19) and (20).

$$J_{hom} = A_{hom} \exp\left(-\frac{16\pi\sigma^3\nu^2}{3K_B^3T^3(lnS)^2}\right) \tag{19}$$

$$J_{het} = A_{het} \exp\left(-\frac{16\pi\sigma_{het}{}^3\nu^2}{3K_B^3T^3(lnS)^2}\right) \tag{20}$$

where A is the pre-exponential factor for heterogeneous and homogeneous nucleation, σ is the interfacial tension, ν is the molecular volume, Kb is the Boltzman constant, and T is the temperature of the system. Heterogeneous and homogeneous nucleation phenomena are dominant for different supersaturation ratios. Heterogeneous nucleation predominates at a lower supersaturation ratio, while homogeneous nucleation prevails at a higher ratio. The determination of the nucleation rate plays an important role in crystal size control. Nevertheless, it is hard to determinate the nucleation rate experimentally. Therefore, it is generally related to the induction time, which is strongly related to the nucleation rate and can be estimated more easily.

The induction time is the period between an initial supersaturation is created and the detection of the formation of the first crystal. The induction time could be defined as the sum of the time for critical nucleus formation and the growth to a detectable size. Therefore, the detection technique plays an important role in the induction time determination. It is often determined visually, turbidimetrically and conductimetrically [42,43]. Thus, as the growth influences the induction time, its determination becomes difficult and some assumptions must be made. First, the supersaturation is established instantaneously and remains constant until the detection of the first crystal, where the crystal size distribution starts to change and reaches a steady-state distribution, which implies the assumption that the nucleation is not so fast or slow. The time of steady-state distribution achievement coincides with the steady-state nucleation rate achievement because the size distribution spans all sizes up to the critical nucleus[43]. Therefore, nucleation rate and induction time can be related through eq. (21).

$$J \approx \frac{1}{t_u} \tag{21}$$

Therefore, by substituting the eq. (21) in eq. (19), the induction time can be expressed as a function of the supersaturation as shown in eq. (22).

$$t_u = A_x \exp\left(\frac{16\pi\sigma^3\nu^2}{3K_B^3T^3(lnS)^2}\right) \tag{22}$$

In such a way, by linearizing the eq. (22), which becomes eq. (23), and plotting the $\log(t_u)$ versus $(\log S)^{-2}$ it is possible to identify the range of the supersaturation ratio where homogeneous nucleation is dominant over heterogeneous nucleation.

$$lnt_u = lnA_x + \left(\frac{16\pi\sigma^3\nu^2}{3K_B^3T^3(lnS)^2}\right) \tag{23}$$

In addition to the influence of the supersaturation and temperature on the induction time, another important factor to consider is the presence of impurities, which will be studied in this work.

1.1.2. Crystal growth

The nucleation step is followed by the crystal growth, constituted by two mechanisms: i) mass transfer of the ions from the bulk solution to the crystal surface and ii) surface integration of the crystal unit in the crystal lattice. Many theories were proposed to explain the mechanism of the surface integration phenomena, such as Volmer, Kossel and Frank's Theory [44].

The growth rate is widely defined as the mean size (L) increase of the crystal per unit of time and can be estimated experimentally through eq. (24). Therefore, by monitoring the variation of the mean size and the saturation level during the time, the growth rate can be related to the absolute saturation (s = S-1) according to eq. (25), which describes an empirical power law where k_g is a kinetics constant, which is related to the temperature, while g is the growth order, which is related to growth controlling step. The use of an empirical power law in the evaluation of experimental data for design purposes is convenient, especially when neither the boundary layer transport resistance nor the surface integration resistance are clearly governing.

$$G = \frac{\Delta L_{mean}}{\Delta t} \tag{24}$$

$$G = k_g s^g \tag{25}$$

High supersaturation ratios have g values equal to 1, i.e., linear growth, while low supersaturation ratios entail a parabolic growth ($g = 2$) [45,46]. In addition, the growth rate follows a linear rate law if it is controlled by surface adsorption. On the other hand, g values that are distant from the unit reflect a crystal growth rate which can be assumed to be controlled by the step when the growth unit is actually integrated into the lattice, i.g. evidence of any surface kinetics limitation[46]. The power law describes the crystal growth dependence with the temperature and supersaturation. Nevertheless, it cannot describe the growth mechanism, which requires investigating and fitting the growth curve to the equations of different growth mechanisms, such as spiral and two-dimensional growth models [47].

2. Experimental and methods

2.1. Materials and methods

For the kinetics study of both nucleation and growth phenomena, anhydrous granular $CaCl_2$, anhydrous powder Na_2CO_3, 99.999% trace metal basis $(NH_4)_2CO_3$ and reagent grade K_2CO_3 were employed to prepare the precursor solutions in deionized water ($\chi = 3$ μS/cm). Two different $CaCO_3$ seeds were employed for the growth tests. First, a commercial $CaCO_3$ provided by Tec Star S.r.l, and a $CaCO_3$ powder synthesized with a procedure reported elsewhere[48]. The characterization of these powders is shown later.

After each test, the crystals were dried and characterized by means of X-ray diffraction, crystal size distribution and morphological analysis.

The phase purity of the samples was examined by X-ray diffraction on a Panalytical PW 3040 X'Pert equipped with a Cu anode for the Kα radiation generation at 40 kV operating voltage in the 2θ range of 20–70° with a scanning step of 0.013° and a radiation CuKα, k = 1.54056 Å. The crystalline phase was identified by employing the Powder Diffraction File PDF-4/Minerals 2020 of JCPDS. The crystal size distribution was determined by employing a Coulter LS 230 laser crystal size analyzer. Ultrasonic agitation (VCX 600 Ultrasonic) was used to obtain well dispersed and agglomerate-free suspensions. The crystal size

distribution (number or volume per cent) of the suspension was produced by the computer-controlled Coulter LS 230 instrument via software. Morphological characterization was obtained using Field Emission Scanning Electron microscopy (ZEISS MERLIN FE-SEM operated at 3 kV). FESEM provides topographical magnifications up to 1 000 000× and produces clear image resolutions down to 1 nm. A TEM-like procedure for FESEM analysis was employed. The samples were prepared for electron microscopy observations by suspending a small amount of nanocrystals in isopropanol, through ultrasonic mixing for 30 min, and subsequently by placing a drop of the dispersion on a copper grid coated with a layer of amorphous carbon. Finally, the sample was dried at room temperature before FESEM analysis.

2.2. Experimental setup and methodology

2.2.1. Induction time estimation

The determination of the induction time and its variation according to the supersaturation ratio were determined by measuring conductivity and pH. The ion activity was calculated according to the Debye-Huckel law. Equalvolumes of $CaCl_2$ and Na_2CO_3 solutions were quickly mixed in an equimolar ratio, i.e. 1:1 and vigorously stirred, as shown in Fig. 1a. The conductivity was continuously monitored. Different initial concentrations were tested and a different carbonate precursor (Na_2CO_3 and $(NH_4)_2CO_3$), in order to study the effect of different supersaturation ratios and ion presence on the nucleation. The pH was also measured to determine the effective concentration of the carbonate ions, according to the equilibria reactions described in eq. (13) and (14), and to determine the supersaturation ratio. The conditions of each test including the initial measured pH of the test (pH_{in}), ionic strength (I), ion activity(γ) and the related supersaturation ratios with respect to the calcite and vaterite solubility product ($k_{sp\text{-}vat} = 1.26 \times 10^{-8}$; $k_{sp\text{-}cal\text{-}} = 3.3 \times 10^{-9}$) are reported in Table 1 and Table 2.

In such a way, it was possible to obtain the change of the induction time against the supersaturation ratio and plot the log(t_u) versus the $(\log S)^{-2}$ to identify the homogeneous and heterogeneous nucleation troughtthe change of the slope between the data. The kinetics parameters were calculated considering the precipitated crystal phase, vaterite or calcite, for the S evaluation. The effective carbonate concentration was estimated through eqs. (26) and (27).

$$CO_2(l) + OH^- \underset{k_{12}}{\overset{k_{11}}{\rightleftharpoons}} HCO_3^- \tag{26}$$

$$HCO_3^- + OH^- \underset{k_{22}}{\overset{k_{21}}{\rightleftharpoons}} CO_3^{2-} + H_2O \tag{27}$$

Table 1
Tests Conditions for induction times measurements with sodium carbonate.

$[CaCl_2]_{in}$ (mmol/L)	$[Na_2CO_3]_{in}$ (mmol/L)	pH_{in}	I (mmol/L)	Log (γ)	S_{cal}	S_{vat}
0.5	0.5	10.13	2.4	−0.09	4	2.2
0.75	0.75	10.3	3.7	−0.11	7	3.5
1	1	10.3	4.9	−0.13	9	4.5
1.5	1.5	10.35	7.4	−0.16	13	6.6
2	2	10.4	10.0	−0.18	16	8.6
2.5	2.5	10.36	12.4	−0.20	19	10.1
3	3	10.5	15.4	−0.22	24	12.4
3.5	3.5	10.52	18.1	−0.23	27	14.1
4	4	10.44	20.3	−0.24	29	15.1
4.5	4.5	10.44	22.8	−0.25	32	16.6
5	5	10.44	25.3	−0.26	35	17.9
5.5	5.5	10.45	27.9	−0.27	37	19.4
6	6	10.46	30.6	−0.28	40	20.8

Table 2
Tests Conditions for induction times measurements with ammonium carbonate.

$[CaCl_2]_{in}$ (mmol/L)	$[(NH_4)_2CO_3]_{in}$ (mmol/L)	pH_{in}	I (mmol/L)	Log (γ)	S_{cal}	S_{vat}
2	2	8.81	0.024	−0.26	3.27	2.1
2.5	2.5	8.89	0.03	−0.28	4.27	2.7
3	3	8.90	0.036	−0.30	4.92	3.2
3.5	3.5	8.89	0.042	−0.32	5.42	3.6
4	4	8.83	0.048	−0.34	5.61	3.7
4.5	4.5	8.78	0.054	−0.35	5.80	3.9
5	5	8.72	0.06	−0.36	5.82	3.9
5.5	5.5	8.69	0.066	−0.37	6.04	4.1
6	6	8.67	0.072	−0.39	6.27	4.2
6.5	6.5	8.61	0.078	−0.40	6.29	4.2
7	7	8.58	0.084	−0.41	6.30	4.3
10	10	8.45	0.12	−0.45	6.99	4.8

2.2.2. Growth kinetics estimation

Fig. 1b shows the experimental setups of the growth tests, where a perfect mixed reactor is employed, containing an initial loading of crystals (seeding), in which only crystal grow takes place, owing to low supersaturations. The PBE described in eq. (18) in which the size-independent growth rate is considered, can be rewritten as a function of the momentum:

$$\frac{dm_k(t)}{dt} = kG(t)m_{k-1}(t) \tag{28}$$

where m_k is the generic momentum of order k, which can be expressed as

$$m_k = \int_0^\infty L^k n(L,t)dL \tag{29}$$

Being the solid concentration balance equation in a fluid-solid

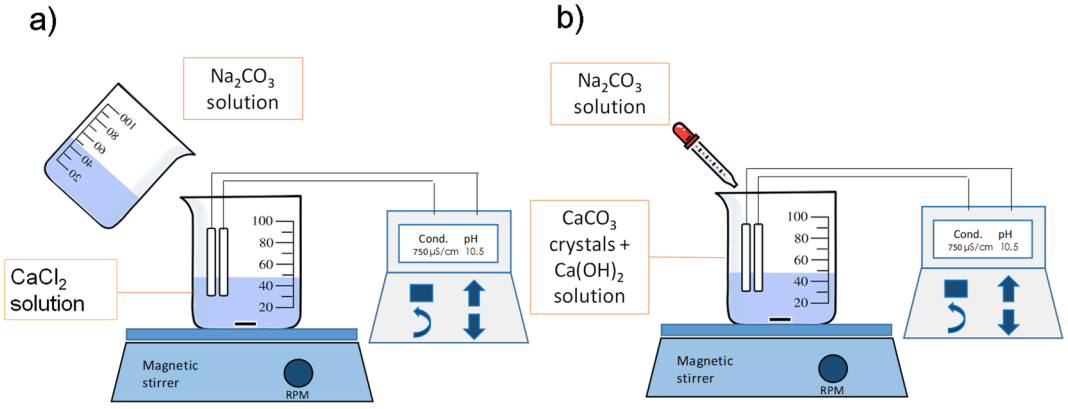

Fig. 1. Experimental setups of a) Nucleation tests b) Growth tests.

system expressed as a function of the m_3 through eq. (30), the mass balance of the solid phase during the precipitation process can be described according to eq. (31).

$$M_T = \rho_c \phi_V \int_0^\infty L^3 n(L,t) dL \tag{30}$$

$$M_{CaCO_3} V_L (C_0 - C(t)) = V_s \phi_V \rho_c \left(m_3(t) - m_{3,0}\right) \tag{31}$$

where M_T is the loading of the suspended solids, ρ_c is the crystal density, ϕ_v is the volumetric shape factor, M_{CaCO_3} is the molar weight of the $CaCO_3$, V_L is the volume of the liquid phase, C_0 is the initial concentration of $CaCO_3$, C(t) is the $CaCO_3$ in the time, V_S is the suspension volume, $m_3(t)$ is the momentum of third-order at time t, and $m_{3,0}$ is the initial momentum of the third order.

Eq. (31) can be derived with respect to time, and the term, dm_3/dt, from the eq. (28) can be substituted in order to obtain the eq. (32), which relates the change of the ion concentration according to the growth rate. The data proceeding can be simplified by employing low concentrations of calcium and carbonate ions, approximately 5% of the initial seeding loading, in order to avoid significant changes in the crystal size distribution and in the surface area of the seeding crystals, which makes it possible to consider m_2 as constant. Since the population density $n(L,t)$ as a function of the mass size distribution is expressed according to eq. (33), the m_2 can be calculated from the initial size distribution through eq. (34). In such a way, the growth rate can be determined by the concentration variation according to eq. (35).

$$-\frac{dC}{dt} = 3\frac{V_s}{M_{CaCO_3} V_L} \phi_V \rho_c m_2 G(t) \tag{32}$$

$$n(L,t) = \frac{m_s}{\varphi_V \rho_C} \frac{g(L,t)}{L^3} \tag{33}$$

$$m_2 \approx m_{2,0} = \frac{C_0 M_{CaCO_3}}{\phi_V \rho_c} I_0, \quad \text{with} \quad = I_0 = \int_0^\infty \frac{g(L,0)}{L} dL \tag{34}$$

$$G(t) = -\frac{dC}{dt} \frac{1}{3 C_0 I_0} \tag{35}$$

The precipitation system consists of a stirred reactor containing the seeding suspension with a known concentration of $Ca(OH)_2$. The system is controlled employing temperature water bath and N_2 atmosphere. The seeding loading was calculated in order to get an increase of the precipitated mass lower than 5%.

Once the temperature was controlled and stable, 5 mL of a concentrated solution of Na_2CO_3/ K_2CO_3/ $(NH_4)_2CO_3$ were rapidly injected in the reactor to have the same concentration of Ca^{2+} and CO_3^{2-} ions. pH and conductivity were continuously recorded to obtain the change of concentration of ions in the solution according to a procedure described elsewhere[49]. Hence, it was possible to correlate the concentration of ions to the growth rate during the test according to eq. (35). After that, a linear regression of the data made it possible to obtain a linearized data for Log G versus Log s and a solution for the linearization of the eq. (25), in which the slope corresponds to the growth order, g and the intercept is the kinetics constant K_g. Table 3 summarizes the operating conditions of the different runs performed to study the crystal growth of $CaCO_3$.

Table 3
Different conditions for kinetic growth tests.

Run	Calcium conc. (mM)	Carbonate conc. (mM)	Carbonate salt	Seed	Seed loading. (mmol/kg)
1	0.2	0.2	Na_2CO_3	micro	25
2	0.2	0.2	K_2CO_3	micro	25
3	0.2	0.2	$(NH_4)_2CO_3$	micro	25
4	0.2	0.2	Na_2CO_3	nano	25
5	0.2	0.2	Na_2CO_3	micro	5
6	0.2	0.2	K_2CO_3	micro	5
7	0.2	0.2	$(NH_4)_2CO_3$	micro	5
8	0.2	0.2	Na_2CO_3	nano	5
9	0.2	0.2	K_2CO_3	nano	5
10	0.5	0.5	Na_2CO_3	micro	25
11	0.3	0.3	Na_2CO_3	micro	25
12	0.1	0.1	Na_2CO_3	micro	25

3. Results and discussion

3.1. Nucleation

The kinetics parameters of the $CaCO_3$ nucleation were determined as explained previously, and the data are reported in the supporting information in section 1 (see figures S1, S2 and S3). The use of different carbonate precursors entailed variations in the kinetics parameters because of different supersaturations for the same initial concentrations. As demonstrated through XRD analysis and FESEM micrographs illustrated in Fig. 2, the nucleation mechanism was noticeably affected. Starting from $NH_4(CO_3)_2$, mainly vaterite was detected, as illustrated in Fig. 2a., while starting from Na_2CO_3, a mixture of calcite and vaterite was obtained as shown in Fig. 2c, according to the vaterite and calcite reference JCPDS card nr. 05-0586 extracted from the PDF-2 database. Naturally, the precipitated vaterite and calcite crystals showed different morphologies. Vaterite had a spherulitic shape formed by very fine crystals, while the calcite crystals showed the classical rhombohedral morphology, as shown in Fig. 2b and c, respectively. These results were expected according to the $CaCO_3$ precipitation mechanism in the presence of Na_2CO_3 described by Rodriguez-Blanco et al.[9], the calcite formation via vaterite. While in the presence of $(NH_4)_2CO_3$, the free NH_4^+ ions tend to interact with the vaterite surface, thus stabilizing the particles and avoiding the transformation into calcite, as reported by some researchers [30–32]. Furthermore, the use of $(NH_4)_2CO_3$ entailed lower pH, which also promotes the formation of vaterite against calcite. Several tests regarding the phase content at different stated pH values were performed and reported in the supporting information (See figure S4). These tests confirmed the effect of the pH on the vaterite and calcite content, indicating that at higher pH (>11) the only formed phase is the calcite. This is in good agreement with Tobler et al. [50], who stated that at high pH values, the precipitation mechanism described is a direct formation of calcite crystals without the vaterite intermediate formation.

The kinetic parameters of eq. (22) were determined by plotting log (t_u) versus $(LnS)^{-2}$ as in eq. (23) (applying a molecular volume of $v = 6.13 \times 10^{-29}$ m3 for calcite and $v = 3.13 \times 10^{-29}$ m^3 for vaterite) and shown in Fig. 3, where it is possible to identify a critical supersaturation ratio equal to 3.8 and 27 when NH_4^+ and Na^+ ions were employed, respectively. For supersaturation ratios higher than these values, homogeneous nucleation is the driving mechanism, while heterogeneous nucleation is dominant at low supersaturation ratios. As reported in Fig. 3, the homogeneous nucleation zone shows a higher slope than the heterogeneous one because of the dependency of this value on the interfacial tension according to eq. (22). In fact, the values for homogeneous nucleation are higher than those for the heterogeneous one and they are the actual interfacial tension values for $CaCO_3$.

The interfacial tension is different for the different $CaCO_3$ crystalline phases [51]. Thus, considering that the crystalline phase in both cases is different, the obtained values of this parameter are different for the different carbonate salts. When $(NH_4)_2CO_3$ was employed as a carbonate source, mainly vaterite precipitated and the values of the interfacial tension of the homogeneous nucleation were lower than those obtained when Na_2CO_3 was employed. In this case, mainly calcite crystals precipitated with a small presence of vaterite crystals, elucidating the calcite precipitation via vaterite, which was not observed with the ammonium carbonate. The value obtained for the vaterite crystals was very similar to the values reported by Gomez-Morales et al.[52] and Verdoes et al.[53], while for the mixture of calcite and vaterite (when Na_2CO_3 was used), the value of the interfacial tension was similar to

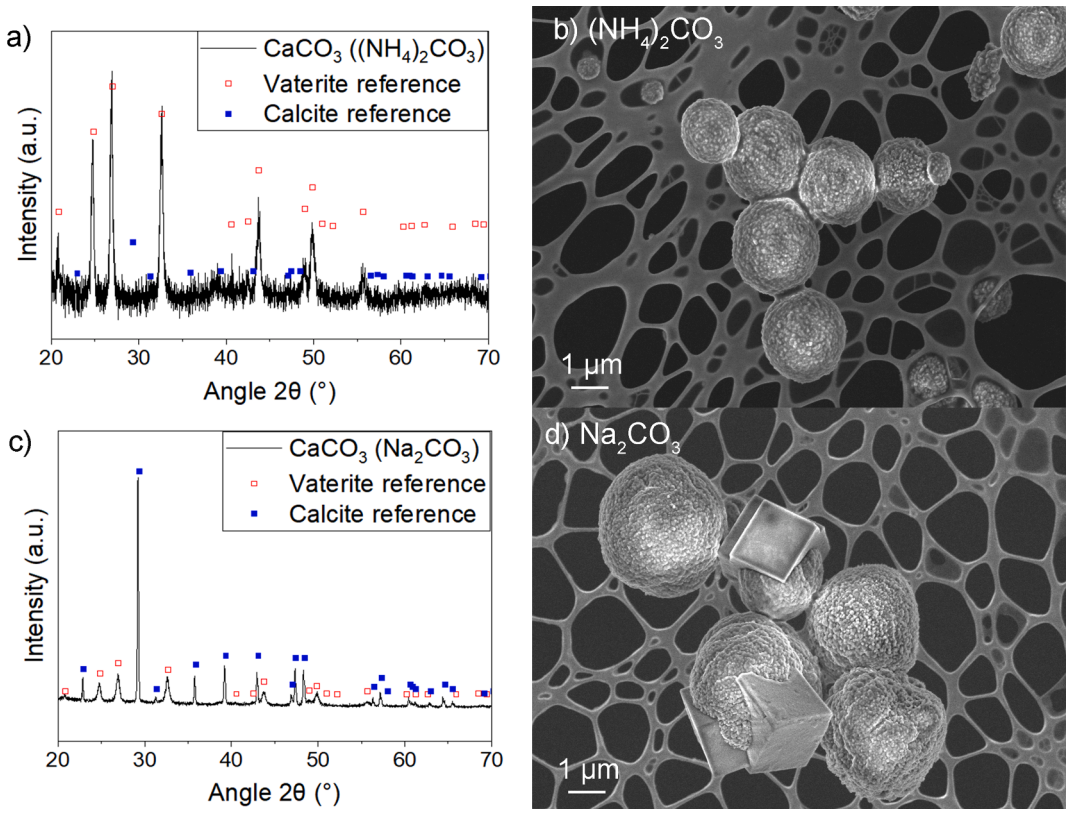

Fig. 2. Characterization of precipitated $CaCO_3$ with ammonium carbonate (a and b) and sodium carbonate (c and d) as CO_3^{2-} source.

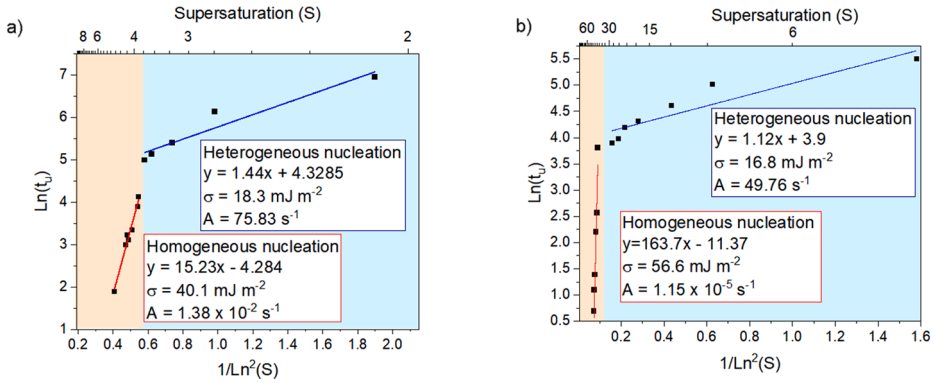

Fig. 3. Homogeneous and heterogeneous nucleation regions and kinetic parameters determination by using ammonium carbonate (a) and sodium carbonate (b) as CO_3^{2-} source.

those found by Flaten et al. [51]. Concerning the pre-exponential factor (reported in Fig. 3), it was considerably larger when $(NH4)_2CO_3$ was employed since it is the supersaturation independent part of the nucleation rate, which, among other factors, reflects the attachment frequency of monomers to the nucleus [54]. Therefore, it is affected by the ions present in the solution because of their different interaction with the crystal surface. The presence of NH_4^+ ions could slightly increase the viscosity, which could also change the diffusivity, directly affecting the A pre-exponential factor and producing a reduction in the nucleation rate [51,55,56]. Therefore, the presence of NH_4^+ ions led to an increase of the A value for homogeneous nucleation. The obtained value is lower than the theoretical expected one, which is very common experimentally.

In the heterogeneous nucleation, the interfacial tension values were similar in both cases and lower than those of the homogeneous one. This might be due to the crystallization of the same phase, the vaterite, starting from both carbonate salts, because milder conditions, low supersaturation levels and pH values (see conditions reported in Table 1 and Table 2), lead the formation of vaterite [50]. Nonetheless, these are not the actual values for vaterite in solution, but they are reduced by the presence of foreign crystals, indicating that the energy barrier to overcome is lower than in the case of homogeneous nucleation [57]. In this case, the pre-exponential factor was affected in the same way; it was higher in the presence of the NH_4^+, explaining the slower nucleation rate. Furthermore, it is important to point out that the slope for the heterogeneous nucleation for $(NH_4)_2CO_3$ was slightly higher. This indicated a slightly faster nucleation rate, which is highlighted in the smaller crystal size shown in the FESEM micrographs of the heterogeneously nucleated crystals illustrated in the supporting information (see figure S5).

3.2. Growth

The tests were performed by employing two different kinds of seeds. Microcrystals and nanocrystals were characterized before tests, and their characterization is shown in Fig. 4. The samples have the same crystalline phase, as shown in Fig. 4 a and b, which shows a pattern that perfectly matches with the calcite reference JCPDS card nr. 05-0586 extracted from PDF-2 database. Unlike the crystalline phase, the crystals mainly differ in size and morphology: the so-called micro seed has a crystal size distribution (CSD), which indicates a mean crystal size equal to 6 μm, reflection of the crystals agglomerates shown in the FESEM micrographs in Fig. 4 e, with a laminated rhombohedral shape. The nano seed has a bimodal CSD with a mean size equal to 2 μm, as shown in Fig. 4 c and d, respectively. The CSD measurement of the nano seed was also affected by agglomeration since the crystals are highly agglomerated, as illustrated in the FESEM micrographs (See Fig. 4 f), which show rhombohedral nano calcite primary crystals. These morphologies are characteristic of calcite, which is the only phase present in these samples.

The kinetic parameters of the crystal growth were determined from the change of pH and conductivity (κ) as elucidated in the section 2 of the supporting information (See figures S6, S7, S8, S9, S10 and S11). Accordingly, the effect of different parameters was evaluated. The initial concentration of Ca^{2+} and CO_3^{2-} ions, i.e. the supersaturation, was varied in order to study its effect on crystal growth kinetics. The growth constant was increased with the supersaturation, as shown in Fig. 5a. At low initial concentrations, 0.1 and 0.2 mmol/L, the growth constant was equal to 4.8×10^{-11} and 3.9×10^{-11} m/s, respectively, with an order $g = 2$. In contrast, at higher initial concentrations, 0.3 and 0.5 mmol/L, it was equal to 2.9×10^{-10} and 1.2×10^{-10} m/s, respectively, with $g = 1$. These results suggested that the crystal growth constant decreased with the initial supersaturation, and a linear model at high supersaturations represents the growth rate. In contrast, a parabolic growth at low supersaturations describes it. These results were expected[45,46] and indicate that $CaCO_3$ growth follows the Burton, Cabrera and Frank (BCF) model [58]. Furthermore, Salvatori et al.[49] obtained the same trend for the growth kinetics of $BaCO_3$ crystals.

Also, the effect of different ions on the growth kinetics was determined. The growth order was 2 for every run. Therefore the parabolic growth indicates a kind of surface kinetic limitation[46]. Ammonium, potassium and sodium carbonate were employed to study the effect of these cations on the crystal growth of $CaCO_3$. Fig. 5b shows the effect of the carbonate salt cation on the crystal growth constant, K_g, by employing two different initial loadings of seed. With a low initial loading of the micro seed (5 mmol/kg), the K_g was reduced by increasing the ionic radius of the cation from the carbonate source ($Na^+ < K^+ <$

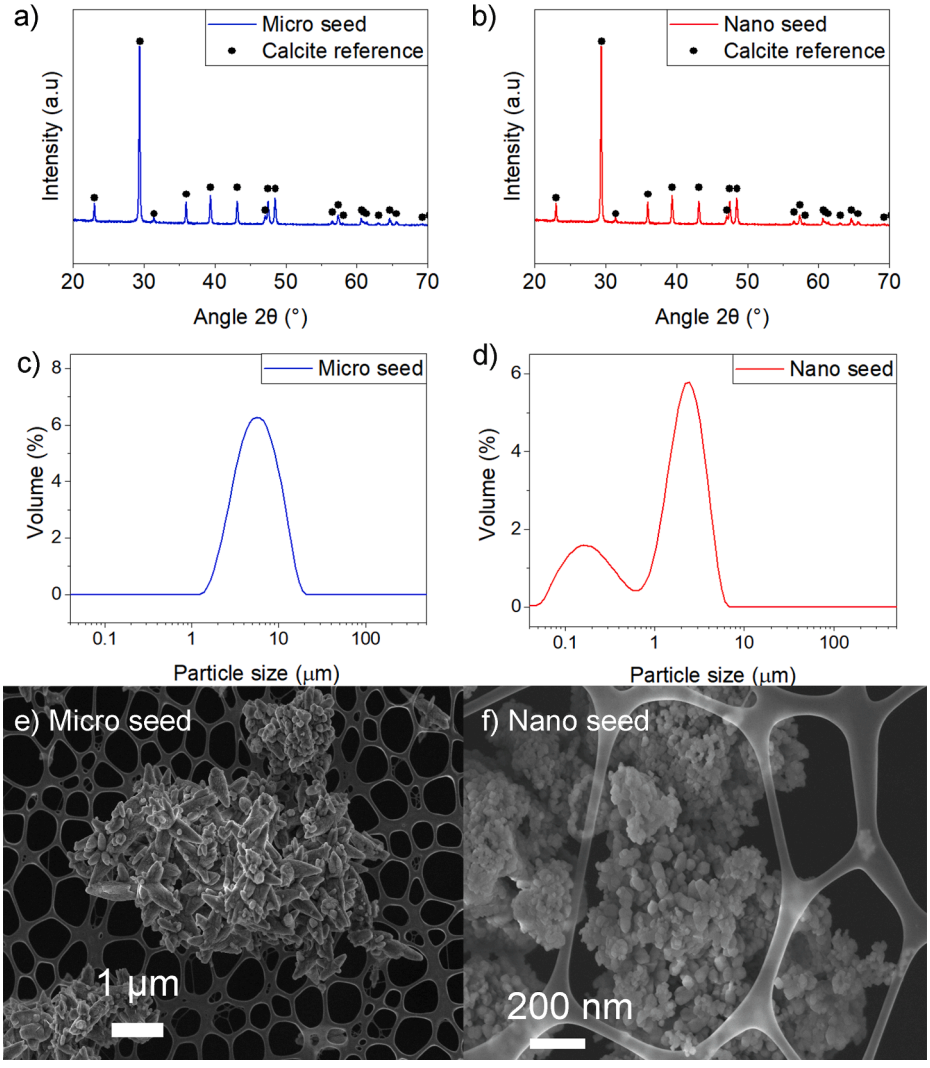

Fig. 4. Seeds characterization. a) Micro seed XRD pattern. b) Nano seed XRD pattern. c) Micro seed CSD. d) Nano seed CSD. e) Micro seed FESEM micrograph. f) Nano seed FESEM micrograph.

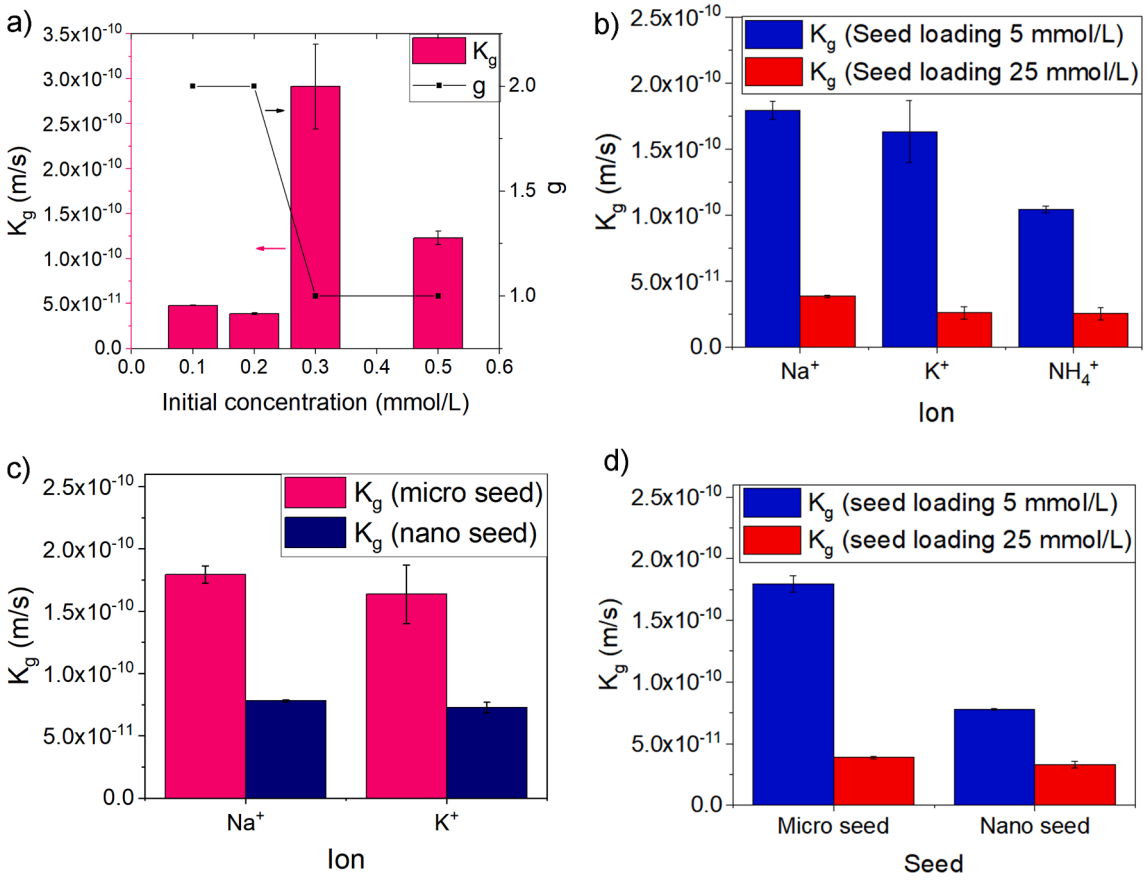

Fig. 5. Operating parameters effects on the $CaCO_3$ growth kinetics. a) Ion and Ca^{2+} and CO_3^{2-} concentration effect (Constant micro seed loading equal to 5 mmol/kg, Na_2CO_3 as CO_3^{2-} source). b) Ion and micro seed loading effect (Constant Ca^{2+} and CO_3^{2-} concentration, 0.2 mM). c) Seed size and CO_3^{2-} source influence (Constant Ca^{2+} and CO_3^{2-} concentration, 0.2 mM and seed loading equal to 5 mmol/kg). d) Seed size and loading (Constant Ca^{2+} and CO_3^{2-} concentration, 0.2 mM; Na_2CO_3 as CO_3^{2-} source).

NH_4^+) due to the small radius of monovalent ions, such as K^+ and Na^+, is suitable for interstitial inclusion of crystals [59,60]. On the other hand, NH_4^+ has a larger ionic radius, which implies that the preferential adsorption of Ca^{2+} on the crystal surface is hindered by NH_4^+ [59]. Likewise, some researchers have found similar results; for instance, Jung et al. [59] determined that the crystal size inversely increased with the ionic radius of the cation. Furthermore, the use of $(NH_4)_2CO_3$ entailed lower ionic strength because of the NH_4^+ hydrolysis, which may reduce the crystal growth rate, according to Tai et al.[61].

For higher loadings of the micro seed, the K_g values obtained were lower, reflecting the results published by Isopescu et al.[62], who observed that the growth rate decreased with the solid loading, i.e. seed loading. Furthermore, the same behaviour concerning the ionic radius of sodium, potassium and ammonium ions was obtained, i.e. slower crystal growth rate in the presence of ammonium ions (see Fig. 5b). Nonetheless, Reddy and Gaillard[63] suggested that the growth constant increases with the seed charge. The highest value of growth constant was obtained by using Na_2CO_3 as CO_3^{2-} ion source and 5 mmol/kg as initial loading of seed, which was equal to 1.8×10^{-10} m/s that is similar to those obtained by Spanos and Koutsoukos [41] and Andreassen and Hounslow[8]. Hence, in general terms, the kinetic parameters reported in this work are very similar to those reported by Verdoes et al.[53] who determined a parabolic growth and a K_g equal to 2.4×10^{-12} m/s. Instead, Flaten et al.[51] who used $CaCl_2$ and Na_2CO_3 established parabolic growth and K_g values between 7.0×10^{-13} and 1.2×10^{-12} m/s. On the other hand, other researchers have obtained K_g values equal to 1×10^{-10} and 5.3×10^{-10} m/s [8,41]. The uncertainty between these results could be caused by the different operating conditions and experimental setups employed for the experiments. The kinetics of precipitation is very sensitive to any environmental parameter [44].

The effect of size is shown in Fig. 5c by employing Na_2CO_3 and K_2CO_3 as CO_3^{2-} source and initial seed loading equal to 5 mmol/kg. The growth constant, K_g, is affected in the same way by the ion, i.e. it was higher by employing smaller ionic radius cation for both seeds, micro and nano sized ones. However, the K_g is smaller for fine crystals (nano seed), which indicated that the assumption of size-independent growth was not respected and that the growth rate was directly proportional to the crystal dimension. Several studies on size dependence of crystal growth, with different crystals, reported that the growth rate increases with the crystal size [40,64–67]. Correspondingly, $CaCO_3$ crystals have previously shown this size-dependence growth in a previous kinetics study conducted by Tai et al.[6]. Also, through carbonation Isopescu et al.[62] studied the precipitation of $CaCO_3$ and determined that the size-dependent growth models predicts very well the CSD at low residence times and low supersaturations, indicating that the growth rate is directly proportional to the crystal size (CS). These results could be due to growth rate dispersion as suggested by Randolph and Larson [68]. Furthermore, results from Tai et al.[6] suggested that the surface integration step is responsible for the size-dependent growth of calcite crystals due to larger crystals are likely to suffer to collisions, causing surface damage and more spiral centers that increase the crystal growth rate. Furthermore, crystals with different dimensions may have different mechanisms in the mass transport process. In fact, Tai et al.[6] also attributed this trend to different mass transport processes for large and small crystals.

The size effect was also studied by employing different initial seed loadings (5 and 25 mmol/kg) and using Na_2CO_3 as the source of CO_3^{2-} ions. The result was very interesting because the growth rate should

decrease with solid loading and smaller crystals, as elucidated before. Nonetheless, results reported in Fig. 5d do not reflect exactly this behaviour. The K_g was reduced by increasing the seed loading from 5 to 25 mmol/kg when micro and nano seed were employed, and at low crystal loading, the crystal growth rate was lower for smaller crystals. Nonetheless, at high crystal loading, the reduction of the K_g was not that evident when smaller crystals were employed. This unexpected behaviour may also be due to probable agglomeration phenomena of the nano seed, which was not taken into consideration in the model. The agglomeration is favored at higher ionic strengths, higher solid loadings and small sizes [69–71]. An increase of the crystal size leads to a higher energy barrier for the agglomeration [71], which agrees with the DLVO theory (named after Derjaguin and Landau, Verwey and Overbeek), which explains the aggregation of the aqueous dispersion and establishes that smaller crystal can agglomerate easily [72]. This is because the fine crystals tend to aggregate to achieve a minimum total surface free energy, owing to their surface free energy [13]. In fact, the micro seed showed higher stability ($|\zeta| > 30$ mV) than the nano seed, which had a zeta potential slightly greater than zero, as shown in the zeta potential measurements reported in the supporting information of this paper (See figures S12, S13, S14 and S15).

Furthermore, the so-called micro seed had a different structure with higher roughness because of its laminated shape. So, the higher crystal growth rate can also be attributed to this shape, since it provides more active sites and edge sites for the kink formation and propagation along the plane (1014), which is the cleavage plane with obtuse and acute step edges dominating equilibrium and growth morphology of calcite [73–75]. Roughness provides a greater surface concentration of step sites available for the integration of new growth units into the lattice [47,76].

4. Conclusions

$CaCO_3$ precipitation kinetics are widely affected by several parameters: ions, seed size, seed loading, and supersaturation. Different ions could interfere to a different order of magnitude according to their ionic radius and its interaction with the crystal surface. Instead, seed size and loading could affect the mass transfer and surface integration. Finally, precipitation kinetics seem to show a strong supersaturation dependence, since the mechanism of nucleation and growth is different at low and high supersaturations.

At low supersaturations, heterogeneous nucleation was predominant, while high supersaturations led to homogeneous nucleation. The nucleation of $CaCO_3$ could be controlled by using different CO_3^{2-} sources and favouring a certain crystal phase or morphology, e.g. $(NH_4)_2CO_3$ promotes the nucleation of vaterite, while the use of Na_2CO_3 will produce mainly calcite crystals. At high initial pH when $(NH_4)_2CO_3$ was used, the formation of vaterite was inhibited, modifying the precipitation mechanism. In addition, the kinetics for both CO_3^{2-} sources were different; the homogeneous nucleation in the presence of Na_2CO_3 was faster than in the presence of $(NH_4)_2CO_3$, while the values of the heterogeneous nucleation were comparable, probably because in this case, the same $CaCO_3$ phase, the vaterite, was obtained.

The power-law model could be employed to study and describe the growth rate. At higher supersaturations, the kinetics order of the crystal growth was 1, while at low supersaturations, it was 2. Furthermore, the growth rate was affected by the presence of different ions. Ions with smaller ionic radius entailed higher growth rates. Nevertheless, the use of different solid loadings and crystal sizes entailed variations of the growth constant of the power law, which indicates, in addition to a size-dependent growth, an influence on mass transfer. Therefore, it could be advisable to employ a two-step model, which could better determine the influence of these parameters. Also, even if the proposed model allows an approximation of the growth rate constant to be obtained, a better determination of this value could be obtained by employing another kinetics model that takes into consideration the size-dependent growth and aggregation phenomena.

CRediT authorship contribution statement

Freddy Liendo: Conceptualization, Data curation, Formal analysis, Investigation, Methodology, Writing – original draft, Writing – review & editing. **Mara Arduino:** Conceptualization, Data curation, Formal analysis, Investigation, Methodology, Writing – original draft, Writing – review & editing. **Fabio A. Deorsola:** Methodology, Supervision, Writing – review & editing. **Samir Bensaid:** Data curation, Project administration, Resources, Supervision, Writing – review & editing.

Declaration of Competing Interest

The authors declare that they have no known competing financial interests or personal relationships that could have appeared to influence the work reported in this paper.

Acknowledgements

This project has received funding from the European Union's Horizon 2020 Research and Innovation Programme under Grant Agreement No. 768583. This paper reflects only the author's view and the content is the sole responsibility of the authors. The European Commission or its services cannot be held responsible for any use that may be made of the information it contains.

Appendix A. Supplementary material

Supplementary data to this article can be found online at https://doi.org/10.1016/j.jcrysgro.2021.126406.

References

[1] Y. Boyjoo, V.K. Pareek, J. Liu, Synthesis of micro and nano-sized calcium carbonate particles and their applications, J. Mater. Chem. A. 2 (35) (2014) 14270–14288, https://doi.org/10.1039/C4TA02070G.
[2] B. Njegić-Džakula, G. Falini, L. Brečević, Ž. Skoko, D. Kralj, Effects of initial supersaturation on spontaneous precipitation of calcium carbonate in the presence of charged poly-l-amino acids, J. Colloid Interface Sci. 343 (2) (2010) 553–563, https://doi.org/10.1016/j.jcis.2009.12.010.
[3] Y. Wen, L. Xiang, Y. Jin, Synthesis of plate-like calcium carbonate via carbonation route, Mater. Lett. 57 (16-17) (2003) 2565–2571, https://doi.org/10.1016/S0167-577X(02)01312-5.
[4] A. Declet, E. Reyes, O.M. Suárez, Calcium carbonate precipitation: A review of the carbonate crystallization process and applications in bioinspired composites, Rev. Adv. Mater. Sci. 44 (2016) 87–107.
[5] M.Y. Memar, K. Adibkia, S. Farajnia, H.S. Kafil, S. Maleki Dizaj, R. Ghotaslou, Biocompatibility, cytotoxicity and antimicrobial effects of gentamicin-loaded CaCO3 as a drug delivery to osteomyelitis, J. Drug Deliv. Sci. Technol. 54 (2019) 101307, https://doi.org/10.1016/j.jddst.2019.101307.
[6] C.Y. Tai, P.-C. Chen, S.-M. Shih, Size-Dependent growth and contact nucleation of calcite crystals, AIChE J. 39 (9) (1993) 1472–1482, https://doi.org/10.1002/aic.v39:910.1002/aic.690390907.
[7] H.N.S. Wiechers, P. Sturrock, G.V.R. Marais, Calcium carbonate crystallization kinetics, Water Res. 9 (1975) 835–845, https://doi.org/10.1016/0043-1354(75)90143-8.
[8] J.-P. Andreassen, M.J. Hounslow, Growth and aggregation of vaterite in seeded-batch experiments, AIChE J. 50 (11) (2004) 2772–2782, https://doi.org/10.1002/(ISSN)1547-590510.1002/aic.v50:1110.1002/aic.10205.
[9] J.D. Rodriguez-Blanco, S. Shaw, L.G. Benning, The kinetics and mechanisms of amorphous calcium carbonate (ACC) crystallization to calcite, via vaterite, Nanoscale. 3 (1) (2011) 265–271, https://doi.org/10.1039/C0NR00589D.
[10] P. Bots, L.G. Benning, J.-D. Rodriguez-Blanco, T. Roncal-Herrero, S. Shaw, Mechanistic insights into the crystallization of amorphous calcium carbonate (ACC), Cryst. Growth Des. 12 (7) (2012) 3806–3814, https://doi.org/10.1021/cg300676b.
[11] T. Ogino, T. Suzuki, K. Sawada, The rate and mechanism of polymorphic transformation of calcium carbonate in water, J. Cryst. Growth. 100 (1-2) (1990) 159–167, https://doi.org/10.1016/0022-0248(90)90618-U.
[12] S. Park, M.G. Lee, J. Park, CO2 (carbon dioxide) fixation by applying new chemical absorption-precipitation methods, Energy. 59 (2013) 737–742, https://doi.org/10.1016/j.energy.2013.07.057.
[13] R. Chang, S. Kim, S. Lee, S. Choi, M. Kim, Y. Park, Calcium carbonate precipitation for CO 2 storage and utilization: A review of the carbonate crystallization and

polymorphism, Front. Energy Res. 5 (2017) 1–12, https://doi.org/10.3389/fenrg.2017.00017.
[14] H.P. Mattila, R. Zevenhoven, Production of Precipitated Calcium Carbonate from Steel Converter Slag and Other Calcium-Containing Industrial Wastes and Residues, first ed, Adv. Inorg. Chem. 66 (2014) 347–384, https://doi.org/10.1016/B978-0-12-420221-4.00010-X.
[15] G. Falini, S. Fermani, G. Tosi, E. Dinelli, Calcium carbonate morphology and structure in the presence of seawater ions and humic acids, Cryst. Growth Des. 9 (5) (2009) 2065–2072, https://doi.org/10.1021/cg8002959.
[16] I.Z. Yildirim, M. Prezzi, Chemical, mineralogical, and morphological properties of steel slag, Adv. Civ. Eng. 2011 (2011) 1–13, https://doi.org/10.1155/2011/463638.
[17] R. Ragipani, S. Bhattacharya, A.K. Suresh, Towards efficient calcium extraction from steel slag and carbon dioxide utilization via pressure-swing mineral carbonation, React. Chem. Eng. 4 (2019) 52–66, https://doi.org/10.1039/c8re00167g.
[18] R.M. Cuéllar-Franca, A. Azapagic, Carbon capture, storage and utilization technologies: A critical analysis and comparison of their life cycle environmental impacts, J. CO2 Util. 9 (2015) 82–102, https://doi.org/10.1016/j.jcou.2014.12.001.
[19] Z. Hu, Y. Deng, Synthesis of needle-like aragonite from calcium chloride and sparingly soluble magnesium carbonate, Powder Technol. 140 (1-2) (2004) 10–16, https://doi.org/10.1016/j.powtec.2004.01.001.
[20] W.K. Park, S.-J. Ko, S.W. Lee, K.-H. Cho, J.-W. Ahn, C. Han, Effects of magnesium chloride and organic additives on the synthesis of aragonite precipitated calcium carbonate, J. Cryst. Growth. 310 (10) (2008) 2593–2601, https://doi.org/10.1016/j.jcrysgro.2008.01.023.
[21] C.R. Blue, A. Giuffre, S. Mergelsberg, N. Han, J.J. De Yoreo, P.M. Dove, Chemical and physical controls on the transformation of amorphous calcium carbonate into crystalline CaCO3 polymorphs, Geochim. Cosmochim. Acta. 196 (2017) 179–196, https://doi.org/10.1016/j.gca.2016.09.004.
[22] C. Ramakrishna, T. Thenepalli, J.W. Ahn, Evaluation of various synthesis methods for calcite-precipitated calcium carbonate (PCC) formation, Korean Chem. Eng. Res. 55 (2017) 279–286, https://doi.org/10.9713/kcer.2017.55.3.279.
[23] Z. Hu, M. Shao, H. Li, Q. Cai, C. Zhong, Z. Xianming, Y. Deng, Synthesis of needle-like aragonite crystals in the presence of magnesium chloride and their application in papermaking, Adv. Compos. Mater. 18 (4) (2009) 315–326, https://doi.org/10.1163/156855109X434720.
[24] M. Wang, H.K. Zou, L. Shao, J.F. Chen, Controlling factors and mechanism of preparing needlelike CaCO3 under high-gravity environment, Powder Technol. 142 (2-3) (2004) 166–174, https://doi.org/10.1016/j.powtec.2004.05.003.
[25] R. Chang, D. Choi, M.H. Kim, Y. Park, Tuning crystal polymorphisms and structural investigation of precipitated calcium carbonates for CO2 mineralization, ACS Sustain. Chem. Eng. 5 (2) (2017) 1659–1667, https://doi.org/10.1021/acssuschemeng.6b0241110.1021/acssuschemeng.6b02411.s001.
[26] Z. Hu, M. Shao, Q. Cai, S. Ding, C. Zhong, X. Wei, Y. Deng, Synthesis of needle-like aragonite from limestone in the presence of magnesium chloride, J. Mater. Process. Technol. 209 (3) (2009) 1607–1611, https://doi.org/10.1016/j.jmatprotec.2008.04.008.
[27] J. Harris, S. Wolf, Desiccator volume: A vital yet ignored parameter in CACO3 crystallization by the ammonium carbonate diffusion method, Minerals. 7 (7) (2017) 122, https://doi.org/10.3390/min7070122.
[28] Y. Zhong, T. Shi, Q. Chen, X. Yang, D. Xu, Z. Zhang, X. Wang, B. Zhong, Leaching calcium from phosphogypsum desulfurization slag by using ammonium chloride solution: Thermodynamics and kinetics study, Chinese, J Chem. Eng. 28 (1) (2020) 208–215, https://doi.org/10.1016/j.cjche.2019.08.006.
[29] H.P. Mattila, H. Hudd, R. Zevenhoven, Cradle-to-gate life cycle assessment of precipitated calcium carbonate production from steel converter slag, J. Clean. Prod. 84 (2014) 611–618, https://doi.org/10.1016/j.jclepro.2014.05.064.
[30] D. Konopacka-Łyskawa, B. Kościelska, M. Łapiński, Precipitation of Spherical Vaterite Particles via Carbonation Route in the Bubble Column and the Gas-Lift Reactor, Jom. 71 (3) (2019) 1041–1048, https://doi.org/10.1007/s11837-018-3307-0.
[31] B. Wang, Z. Pan, H. Cheng, Z. Chen, F. Cheng, High-yield synthesis of vaterite microparticles in gypsum suspension system via ultrasonic probe vibration/magnetic stirring, J. Cryst. Growth. 492 (2018) 122–131, https://doi.org/10.1016/j.jcrysgro.2018.02.021.
[32] Q. Hu, J. Zhang, H. Teng, U. Becker, Growth process and crystallographic properties of ammonia-induced vaterite, Am. Mineral. 97 (8-9) (2012) 1437–1445, https://doi.org/10.2138/am.2012.3983.
[33] I. Udrea, C. Capat, E.A. Olaru, R. Isopescu, M. Mihai, C.D. Mateescu, C. Bradu, Vaterite synthesis via gas-liquid route under controlled pH conditions, Ind. Eng. Chem. Res. 51 (24) (2012) 8185–8193, https://doi.org/10.1021/ie202221m.
[34] D. Konopacka-Łyskawa, Synthesis methods and favorable conditions for spherical vaterite precipitation: A review, Crystals. 9 (4) (2019) 223, https://doi.org/10.3390/cryst9040223.
[35] O. Velts, M. Hautaniemi, J. Kallas, R. Kuusik, Modeling calcium dissolution from oil shale ash: Part 1. Ca dissolution during ash washing in a batch reactor, Fuel Process. Technol. 91 (5) (2010) 486–490, https://doi.org/10.1016/j.fuproc.2009.12.008.
[36] J.-H. Bang, Y. Yoo, S.-W. Lee, K. Song, S. Chae, Co2 mineralization using brine discharged from a seawater desalination plant, Minerals. 7 (11) (2017) 207, https://doi.org/10.3390/min7110207.
[37] J. Jeon, M.-J. Kim, CO2 storage and CaCO3 production using seawater and an alkali industrial by-product, Chem. Eng. J. 378 (2019) 122180, https://doi.org/10.1016/j.cej.2019.122180.
[38] K.L. Core, J.C. Mulligan, Heat transfer and population characteristics of dispersed evaporating droplets, AIChE J. 36 (8) (1990) 1137–1144.
[39] C.F. Abegg, Analysis of crystal size distributions when growth rate is size dependent, 1966.
[40] J. Mydlarz, A.G. Jones, On the estimation of size-dependent crystal growth rate functions in MSMPR crystallizers, Chem. Eng. J. Biochem. Eng. J. 53 (2) (1993) 125–135, https://doi.org/10.1016/0923-0467(93)85003-E.
[41] N. Spanos, P.G. Koutsoukos, Kinetics of Precipitation of Calcium Carbonate in Alkaline pH at Constant Supersaturation. Spontaneous and Seeded Growth, J. Phys. Chem. B. 102 (34) (1998) 6679–6684, https://doi.org/10.1021/jp981171h.
[42] O. Sohnel, J.W. Mullin, Precipitation Of Calcium Carbonate, Company, North-Holl. Publ. 60 (1982) 239–250.
[43] O. Söhnel, J.W. Mullin, Interpretation of Crystallization Induction Periods, J. Colloid Interface Sci. 123 (1) (1988) 43–50.
[44] J.W. Mullin, Crystallization, Butterworth-Keinemann, Oxford, 2001.
[45] L.-D. Shiau, Determination of the nucleation and growth kinetics for aqueous L-glycine solutions from the turbidity induction time data, Crystals. 8 (11) (2018) 403, https://doi.org/10.3390/cryst8110403.
[46] K.M. Forsberg, Å.C. Rasmuson, Crystal growth kinetics of iron fluoride trihydrate, J. Cryst. Growth. 296 (2) (2006) 213–220, https://doi.org/10.1016/j.jcrysgro.2006.08.035.
[47] T.D. Dincer, M.I. Ogden, G.M. Parkinson, Crystal growth mechanisms of the (0 1 0) face of α-lactose monohydrate crystals, J. Cryst. Growth. 311 (8) (2009) 2427–2432, https://doi.org/10.1016/j.jcrysgro.2009.02.030.
[48] I. Cosentino, G.A. Ferro, L. Restuccia, S. Bensaid, F. Deorsola, F. Liendo, Nearly zero CO 2 cementitious composites, Mater. Des. Process. Commun. (2019) 1–5, https://doi.org/10.1002/mdp2.125.
[49] F. Salvatori, H. Muhr, E. Plasari, J.-M. Bossoutrot, Determination of nucleation and crystal growth kinetics of barium carbonate, Powder Technol. 128 (2-3) (2002) 114–123, https://doi.org/10.1016/S0032-5910(02)00184-5.
[50] D.J. Tobler, J.D. Rodriguez Blanco, H.O. Sørensen, S.L.S. Stipp, K. Dideriksen, Effect of pH on Amorphous Calcium Carbonate Structure and Transformation, Cryst. Growth Des. 16 (8) (2016) 4500–4508, https://doi.org/10.1021/acs.cgd.6b0063010.1021/acs.cgd.6b00630.s001.
[51] E.M. Flaten, M. Seiersten, J.-P. Andreassen, Induction time studies of calcium carbonate in ethylene glycol and water, Chem. Eng. Res. Des. 88 (12) (2010) 1659–1668, https://doi.org/10.1016/j.cherd.2010.01.028.
[52] J. Gómez-Morales, J. Torrent-Burgués, R. Rodríguez-Clemente, Nucleation of calcium carbonate at different initial pH conditions, J. Cryst. Growth. 169 (2) (1996) 331–338, https://doi.org/10.1016/S0022-0248(96)00381-8.
[53] D. Verdoes, D. Kashchiev, G.M. van Rosmalen, Determination of nucleation and growth rates from induction times in seeded and unseeded precipitation of calcium carbonate, J. Cryst. Growth. 118 (3-4) (1992) 401–413, https://doi.org/10.1016/0022-0248(92)90089-2.
[54] C.P.M. Roelands, J.H. ter Horst, H.J.M. Kramer, P.J. Jansens, Analysis of nucleation rate measurements in precipitation processes, Cryst. Growth Des. 6 (6) (2006) 1380–1392, https://doi.org/10.1021/cg050678w10.1021/cg050678w.s001.
[55] J.W. Mullin, C.L. Leci, Evidence of molecular cluster formation in supersaturated solutions of citric acid, Philos. Mag. A J. Theor. Exp. Appl. Phys. 19 (161) (1969) 1075–1077, https://doi.org/10.1080/14786436908225872.
[56] Y. Shirai, K. Nakanishi, R. Matsuno, T. Kamikubo, Effects of Polymers on Secondary Nucleation of Ice Crystals, J. Food Sci. 50 (1985) 401–406, https://doi.org/10.1111/j.1365-2621.1985.tb13412.x.
[57] C. Brandel, J.H. Ter Horst, Measuring induction times and crystal nucleation rates, Faraday Discuss. 179 (2015) 199–214, https://doi.org/10.1039/c4fd00230j.
[58] W.K. Burton, N. Cabrera, F.C. Frank, The growth of crystals and the equilibrium structure of their surfaces, Philos. Trans. R. Soc. London. Ser. A, Math. Phys. Sci. 243 (1951) 299–358. https://doi.org/10.1098/rsta.1951.0006.
[59] T. Jung, W.-S. Kim, C.K. Choi, Effect of monovalent salts on morphology of calcium carbonate crystallized in Couette-Taylor reactor, Cryst. Res. Technol. 40 (6) (2005) 586–592, https://doi.org/10.1002/(ISSN)1521-407910.1002/crat.v40:610.1002/crat.200410387.
[60] M. Okumura, Y. Kitano, Coprecipitation of alkali metal ions with calcium carbonate, Geochim. Cosmochim. Acta. 50 (1986) 49–58.
[61] C.Y. Tai, M. Chang, C. Wu, Y. Lin, Interpretation of calcite growth data using the two-step crystal growth model, Chem. Eng. Sci. 61 (2006) 5346–5354, https://doi.org/10.1016/j.ces.2006.03.047.
[62] R. Isopescu, M. Mocioi, F. Zahanagiu, L. Filipescu, Growth rate models and kinetics estimation for CaCO3 precipitated in continuous crystallizers, J. Cryst. Growth. 167 (1-2) (1996) 260–264, https://doi.org/10.1016/0022-0248(96)00088-7.
[63] M.M. Reddy, W.D. Gaillard, Kinetics of calcium carbonate (calcite)-seeded crystallization: Influence of solid/solution ratio on the reaction rate constant, J. Colloid Interface Sci. 80 (1) (1981) 171–178, https://doi.org/10.1016/0021-9797(81)90173-9.
[64] J. Garside, S.J. Jančić, Growth and dissolution of potash alum crystals in the subsieve size range, AIChE J. 22 (5) (1976) 887–894, https://doi.org/10.1002/(ISSN)1547-590510.1002/aic.v22:510.1002/aic.690220512.
[65] J.W. Mullin, The Crystallization of Aluminium Potassium Sulphate : A Study in the Assessment of Crystallizer Design Data Part II: Growth in a Fluidized Bed Crystallizer, 1967.
[66] A.G. Jones, J. Mydlarz, Continuous crystallization of potash alum: MSMPR kinetics, Can. J. Chem. Eng. 68 (2) (1990) 250–259, https://doi.org/10.1002/cjce:v68:210.1002/cjce:5450680210.
[67] I. Molnár, S. Halász, T. Blickle, Determination of size-dependent crystal growth characteristics from batch experiments, Chem. Eng. Sci. 45 (5) (1990) 1243–1251.

[68] A. Randolph, M. Larson, Theory of particulate processes: analysis and techniques of continuous crystallization, Elsevier, New York, 2012.
[69] O. Söhnel, J.W. Mullin, A.G. Jones, O. Söhnel, Crystallization and Agglomeration Kinetics in the Batch Precipitation of Strontium Molybdate, Ind. Eng. Chem. Res. 27 (1988) 1721–1728, https://doi.org/10.1021/ie00081a026.
[70] A.F. Blandin, D. Mangin, A. Rivoire, J.P. Klein, J.M. Bossoutrot, Agglomeration in suspension of salicylic acid fine particles: Influence of some process parameters on kinetics and agglomerate final size, Powder Technol. 130 (2003) 316–323, https://doi.org/10.1016/S0032-5910(02)00210-3.
[71] D. Zhou, Z. Ji, X. Jiang, D.R. Dunphy, J. Brinker, A.A. Keller, W.-C. Chin, Influence of material properties on TiO2 Nanoparticle agglomeration, PLoS ONE 8 (11) (2013) e81239, https://doi.org/10.1371/journal.pone.0081239.
[72] D. Horinek, DLVO Theory, in: G. Kreysa, K. Ota, R.F. Savinell (Eds.), Encycl. Appl. Electrochem., Springer New York, New York, NY, 2014: pp. 343–346. https://doi.org/10.1007/978-1-4419-6996-5_7.
[73] M. Wolthers, G. Nehrke, J.P. Gustafsson, P. Van Cappellen, Calcite growth kinetics: Modeling the effect of solution stoichiometry, Geochim. Cosmochim. Acta. 77 (2012) 121–134, https://doi.org/10.1016/j.gca.2011.11.003.
[74] J. Paquette, R.J. Reeder, Relationship between surface structure, growth mechanism, and trace element incorporation in calcite, Geochim. Cosmochim. Acta 59 (1995) 735–749.
[75] S.L. Stipp, Structure and bonding environments at the calcite surface as observed with X-ray photoelectron spectroscopy (XPS) and low energy electron diffraction (LEED), Geochim. Cosmochim. Acta 55 (1991) 1723–1736.
[76] J. Ulrich, M. Kruse, GRD and Effects of Surface Quality, a better Explanation than Size-Dependent Growth, proceedings, in: 11th Symp. Ind. Cryst., 1990, pp. 361–366.